

# Optimized holographic optical traps

Marco Polin, Kosta Ladavac,\* Sang-Hyuk Lee, Yael Roichman, and David G. Grier  
*Dept. of Physics and Center for Soft Matter Research, New York University, New York, NY 10003*  
 (Dated: October 8, 2018)

Holographic optical traps use the forces exerted by computer-generated holograms to trap, move and otherwise transform mesoscopically textured materials. This article introduces methods for optimizing holographic optical traps' efficiency and accuracy, and an optimal statistical approach for characterizing their performance. This combination makes possible real-time adaptive optimization.

A single laser beam brought to a focus with a strongly converging lens forms a type of optical trap widely known as an optical tweezer [1]. Multiple beams of light passing simultaneously through the lens' input pupil yield multiple optical tweezers, each at a location determined by its beam's angle of incidence and degree of collimation at the input pupil. The trap-forming laser beams form an interference pattern as they pass through the input pupil, whose amplitude and phase corrugations characterize the downstream trapping pattern. Imposing the same modulations on a single incident beam at the input pupil would yield the same pattern of traps. Such wavefront modification can be performed by a computer-designed diffractive optical element (DOE) commonly known as a hologram.

Holographic optical trapping (HOT) uses methods of computer-generated holography (CGH) to project arbitrary configurations of optical traps [2, 3, 4, 5, 6], with manifold applications in the physical and biological sciences as well as in industry [7]. This flexible approach to manipulating and transforming mesoscopic matter has been used to assemble two- and three-dimensional structures, to sort objects ranging in size from nanoclusters to living cells, and to create all-optical microfluidic pumps and mixers.

This article describes refinements of the HOT technique that help to optimize the traps' performance, as well as a statistically optimal analysis for rapidly characterizing them. Section I describes modifications to the basic HOT optical train that minimize defects due to limitations of practical implementations. Section II discusses a direct search algorithm for HOT DOE computation that is both faster and more accurate than iterative refinement algorithms. A method for rapidly characterizing each trap in a holographic array is presented in Section III. The optimal statistical methods on which this characterization technique is based lends itself naturally to digital video analysis of optically trapped spheres and can be exploited for real-time optimization. Such adaptive optimization is demonstrated experimentally in Section IV.

## I. IMPROVED OPTICAL TRAIN

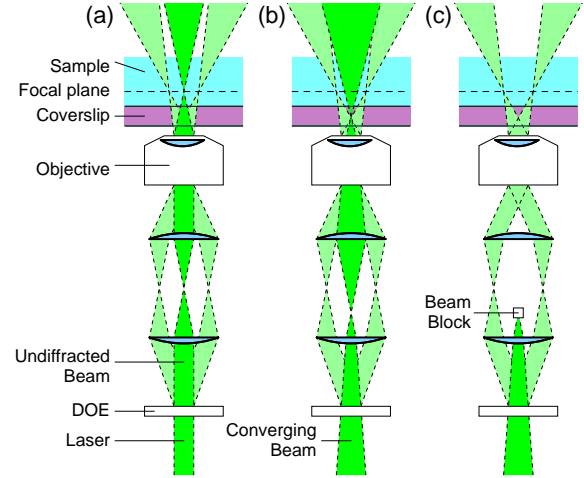


FIG. 1: Simplified schematic of a holographic optical tweezer optical train before and after modification. (a) A collimated beam is split into multiple beams by the DOE, each of which is shown here as being collimated. The diffracted beams pass through the input pupil of an objective lens and are focused into optical traps in the objective's focal plane. The undiffracted portion of the beam, shown here with the darkest shading, also focuses into the focal plane. (b) The input beam is converging as it passes through the DOE. The DOE collimates the diffracted beams, so that they focus into the focal plane, as in (a). The undiffracted beam comes to a focus within the coverslip bounding the sample. (c) A beam block can eliminate the undiffracted beam without substantially degrading the optical traps.

Figure 1(a) shows a simplified schematic of a conventional HOT implementation. A collimated laser beam is imprinted with a CGH and thereafter propagates as a superposition of independent beams, each with individually specified wavefront characteristics [4, 6]. These beams are relayed to the input aperture of a high-numerical-aperture lens, typically a microscope objective, that focuses them into optical traps. This figure indicates a transmissive DOE, although comparable results are obtained with reflective DOE's. The same objective lens used to form the optical traps also can be used to create images of trapped objects. The associated illumination and image-forming optics are omitted from Fig. 1 for clarity. Practical holograms only diffract a portion

\*Department of Physics, James Franck Institute and Institute for Biophysical Dynamics, The University of Chicago, Chicago, IL 60637

of the incident light into intended modes and directions. Some of the incident beam is not diffracted at all, and the undiffracted portion typically forms an unwanted trap in the middle of the field of view [8]. This “central spot” has been removed in previous studies by spatially filtering the diffracted beam [8, 9]. Practical DOE’s also tend to project spurious “ghost” traps into symmetry-dictated positions within the sample. Spatially filtering a large number of ghost traps generally is not practical, particularly in the case of dynamic holographic optical tweezers whose traps move freely in three dimensions. Projecting holographic traps in the off-axis Fresnel geometry, rather than the Fraunhofer geometry described here, automatically eliminates the central spot [10], but limits the number of traps that can be projected, and also does not address the formation of ghost traps.

Figure 1(b) shows one simple improvement to the basic HOT design that minimizes the central spot’s influence and effectively eliminates ghost traps. Here, the source laser beam is converging as it passes through the DOE. As a result, the undiffracted central spot focuses upstream of the objective’s normal focal plane. The degree of collimation of each diffracted beam, and thus the axial position of the resulting trap, can be adjusted by incorporating wavefront-shaping phase functions into the hologram’s design [6], thereby returning the traps to the focal volume. This simple expedient allows the central spot to be projected into the coverslip bounding a sample, rather than the sample itself, thereby ensuring that the undiffracted beam lacks both the intensity and the gradients needed to influence a sample’s dynamics.

An additional consequence of the traps’ displacement relative to the converging beam’s focal point is that the majority of ghost traps are projected to the far side of this point, and therefore out of the sample volume altogether. This is a substantial improvement for processes such as optical fractionation [11, 12], which rely on a precisely specified optical potential energy landscape.

Even though the undiffracted beam may not create an actual trap in this modified optical train, it still can exert radiation pressure on the region of the sample near the center of the field of view. This is a particular problem for large arrays of optical traps in that the central spot can be brighter than the intended traps. Illuminating the DOE with a diverging beam [13] reduces the undiffracted beam’s influence by projecting some of its light out of the optical train. In a thick sample, however, this has the deleterious effect of projecting both the weakened central spot and the undiminished ghost traps into the sample.

These problems all can be mitigated by placing a beam block as shown in Fig. 1(c) in the intermediate focal plane within the relay optics to spatially filter the undiffracted portion of the beam. Because the trap-forming beams come to a focus in a different plane, they are only slightly occluded by the beam block, even if they pass directly along the optical axis. The effect of this occlusion is minimal for conventional optical tweezers and can be

compensated by increasing their relative brightness.

## II. ITERATIVE AND DIRECT SEARCH ALGORITHMS FOR HOT CALCULATION

Holographic optical tweezers’ efficacy is determined by the quality of the trap-forming DOE, which in turn reflects the performance of the algorithms used in their computation. Previous studies have applied holograms calculated by simple linear superposition of the input fields [3], with best results being obtained with random relative phases [4, 6], or with variations [4, 5, 6] on the classic Gerchberg-Saxton and Adaptive-Additive algorithms [14]. Despite their general efficacy, these algorithms yield traps whose relative intensities can differ greatly from their design values, and typically project an unacceptably large fraction of the input power into ghost traps. These problems can become acute for complicated three-dimensional trapping patterns, particularly when the same hologram also is used as a mode converter to project multifunctional arrays of optical traps [4, 6]. This section describes faster and more effective algorithms for HOT DOE calculation based on direct search and simulated annealing.

The holograms used for holographic optical trapping typically operate only on the phase of the incident beam, and not its amplitude. Such phase-only holograms, also known as kinoforms, are far more efficient than amplitude-modulating holograms, which necessarily divert light away from the traps. Quite general trapping patterns can be achieved with kinoforms because optical tweezers rely for their operation on intensity gradients but not on phase variations. The challenge is to find a phase pattern in the input plane that encodes the desired intensity pattern in the focal volume.

According to scalar diffraction theory, the complex field  $E(r, \psi)$ , in the focal plane of a lens of focal length  $f$  is related to the field,  $u(\vec{\rho}) \exp(i\varphi(\vec{\rho}))$ , in its input plane by a Fraunhofer transform,

$$E(\vec{r}) = \int u(\vec{\rho}) \exp(i\varphi(\vec{\rho})) \exp\left(-i\frac{k\vec{r} \cdot \vec{\rho}}{2f}\right) d^2\rho, \quad (1)$$

where  $u(\vec{\rho})$  and  $\varphi(\vec{\rho})$  are the real-valued amplitude and phase, respectively, of the field at position  $\vec{\rho}$  in the input pupil, and  $k = 2\pi/\lambda$  is the wavenumber of light of wavelength  $\lambda$ .

If  $u(\vec{\rho})$  is the amplitude profile of the input laser beam, then  $\varphi(\vec{\rho})$  is the kinoform encoding the pattern. Most practical DOEs, including those projected with SLMs, consist of an array  $\vec{\rho}_j$  of discrete phase pixels, each of which can impose any of  $P$  possible discrete phase shifts  $\varphi_j \in \{0, \dots, \phi_{P-1}\}$ . The field in the focal plane due to such an  $N$ -pixel DOE is, therefore,

$$E(\vec{r}) = \sum_{j=1}^N u_j \exp(i\varphi_j) T_j(\vec{r}), \quad (2)$$

where the transfer matrix describing the light's propagation from input plane to output plane is

$$T_j(\vec{r}) = \exp\left(-i \frac{k\vec{r} \cdot \vec{\rho}_j}{2f}\right). \quad (3)$$

Unlike more general holograms, the desired field in the output plane of a holographic optical trapping system consists of  $M$  discrete bright spots located at  $\vec{r}_m$ :

$$E(\vec{r}) = \sum_{m=1}^M E_m(\vec{r}), \quad \text{with} \quad (4)$$

$$E_m(\vec{r}) = \alpha_m \delta(\vec{r} - \vec{r}_m) \exp(i\xi_m), \quad (5)$$

where  $\alpha_m$  is the relative amplitude of the  $m$ -th trap, normalized by  $\sum_{m=1}^M |\alpha_m|^2 = 1$ , and  $\xi_m$  is its (arbitrary) phase. Here  $\delta(\vec{r})$  represents the amplitude profile of the focused beam of light, which may be treated at least heuristically as a two-dimensional Dirac delta function. The design challenge is to solve Eqs. (2), (3) and (4) for the set of phase shifts  $\varphi_j$  yielding the desired amplitudes  $\alpha_m$  at the correct locations  $\vec{r}_m$ , given  $u_j$  and  $T_j(\vec{r}_m)$ .

The Gerchberg-Saxton algorithm and its generalizations, such as the adaptive-additive algorithm, iteratively solve both the forward transform described by Eqs. (2) and (3), and also its inverse, taking care at each step to converge the calculated amplitudes at the output plane to the design amplitudes and to replace the back-projected amplitudes,  $u_j$ , at the input plane with the laser's actual amplitude profile. Appropriately updating the calculated input and output amplitudes at each cycle can cause the DOE phase  $\varphi_j$  to converge to an approximation to the ideal kinoform, with monotonic convergence possible for some variants [14]. The forward and inverse transforms mapping the input and output planes to each other typically are performed by fast Fourier transform (FFT). Consequently, the output positions  $\vec{r}$  are discretized in units of the Nyquist spatial frequency. The output field, furthermore, is calculated not only at the intended positions of the traps, but also at the spaces between them. This is useful because the process not only maximizes the fraction of the input light diffracted into the desired locations, but also minimizes the intensity of stray light elsewhere. The down side to this is the additional computational cost for computing fields in otherwise uninteresting places.

FFT-based iterative algorithms have additional drawbacks for computing three-dimensional arrays of optical tweezers, or mixtures of more general types of traps. To see this, we review how a beam-splitting DOE can be generalized to include wavefront-shaping capabilities. A diverging or converging beam at the input aperture comes to a focus and forms a trap downstream or upstream of the focal plane, respectively. Its wavefront at the input plane is characterized by the parabolic phase profile

$$\varphi_z(\vec{\rho}, z) = \frac{k\rho^2 z}{f^2}, \quad (6)$$

where  $z$  is the focal spot's displacement along the optical axis relative to the lens' focal plane. This phase profile can be used to move an optical trap relative to the focal plane even if the input beam is collimated by appropriately augmenting the transfer matrix:

$$T_j^z(\vec{r}) = T_j(\vec{r}) K_j^z, \quad (7)$$

where the displacement kernel is

$$K_j^z = \exp(i\varphi_z(\vec{\rho}_j, z)). \quad (8)$$

The result,  $T_j^z(\vec{r})$ , replaces  $T_j(\vec{r})$  as the kernel of Eq. (2).

Similarly, a conventional TEM<sub>00</sub> beam can be converted into a helical mode through

$$\varphi_\ell(\vec{\rho}) = \ell\theta, \quad (9)$$

where  $\theta$  is the azimuthal angle around the optical axis and  $\ell$  is known as the topological charge. Such corkscrew-like beams focus to ring-like optical traps known as optical vortices, which can exert torques as well as forces. The topology-transforming kernel  $K_j^\ell = \exp(i\varphi_\ell(\vec{\rho}_j))$  can be composed with the transfer matrix in the same manner as the displacement-inducing  $K_j^z$ . A variety of analogous phase-based mode transformations have been described, each with applications to single-beam optical trapping [7]. All can be implemented with appropriate transformation kernels. Moreover, different transformation operations can be applied to each beam in a holographic trapping pattern independently, resulting in general three-dimensional configurations of diverse types of optical traps [6].

Calculating the phase pattern  $\varphi_j$  encoding multifunctional three-dimensional optical trapping patterns requires only a slight elaboration. The primary requirement is to measure the actual intensity projected by  $\varphi_j$  into the  $m$ -th trap at its focus. If the associated diffraction-generated beam has a non-trivial wavefront, then it need not create a bright spot at its focal point. On the other hand, if we assume that  $\varphi_j$  creates the required type of beam for the  $m$ -th trap through a phase modulation described by the transformation kernel  $K_{j,m}$ , then applying the inverse operator,  $K_{j,m}^{-1}$ , in Eq. (2) would restore the focal spot. This principle was first applied to creating three dimensional trap arrays [4] in which separate translation kernels were used to project each desired optical tweezer back to the focal plane as an intermediate step in each iterative refinement cycle. Computing the light projected into each plane of traps in this manner involves a separate Fourier transform for the entire plane [4].

Much of this effort is eliminated by computing the field only at the traps' positions, as

$$E_m(\vec{r}_m) = \sum_{j=1}^N K_{j,m}^{-1} T_j(\vec{r}_m) \exp(i\varphi_j), \quad (10)$$

and comparing the resulting amplitudes  $\alpha_m = |E_m|$  with the design values [6]. Unlike the FFT-based approach,

this per-trap algorithm does not directly optimize the field between the traps. However, it also eliminates the need to account for interplane propagation. Moreover, if the values of  $\alpha_m$  match the design values, no light is left over to create ghost traps.

The per-trap calculation suffers from its own shortcomings. The only adjustable parameters in Eqs. (5) and (10) are the relative phases  $\xi_m$  of the projected traps. These  $M - 1$  real-valued parameters must be adjusted to optimize the choice of discrete-valued phase shifts,  $\varphi_j$ , subject to the constraint that the amplitude profile  $u_j$  matches the input laser's. With so few free parameters, however, finding an optimal hologram is not likely.

Equation (10) suggests an alternative approach for computing DOE functions for discrete HOT patterns. The operator  $K_{j,m}^{-1} T_j(\vec{r}_m)$  describes how light in the mode of the  $m$ -th trap propagates from position  $\vec{\rho}_j$  on the DOE to the trap's projected position  $\vec{r}_m$  in the lens' focal plane. If we were to change the DOE's phase  $\varphi_j$  at that point, then the superposition of rays composing the field at  $\vec{r}_m$  would be affected. If the change improves the overall trapping pattern, then we would be inclined to retain it, and seek other such improvements. If, instead, the result were less good, we would restore  $\varphi_j$  to its former value and look elsewhere. This is the basis for direct search algorithms.

The simplest direct search involves selecting a pixel at random from a trial phase pattern, changing its value to any of the  $P - 1$  alternatives, and computing the effect on the projected field. This operation can be performed efficiently by calculating only the changes at the  $M$  traps' positions. The updated trial amplitudes then are compared with their design values and the proposed change is accepted if the overall error is reduced. The process is repeated until the result converges to the design or the acceptance rate for proposed changes dwindles.

A successful and efficient direct search requires an effective assessment of errors. The standard cost function,  $\chi^2 = \sum_{m=1}^M (I_m - \epsilon I_m^{(D)})^2$ , assesses the mean-squared deviations of the  $m$ -th trap's projected intensity  $I_m = |\alpha_m|^2$  from its design value  $I_m^{(D)}$ , assuming an overall diffraction efficiency of  $\epsilon$ . It requires an accurate estimate for  $\epsilon$  and places no emphasis on uniformity in the projected traps' intensities. An alternative proposed by Meister and Winfield [15],

$$C = -\langle I \rangle + f\sigma, \quad (11)$$

avoids both shortcomings. Here,  $\langle I \rangle$  is the mean intensity at the traps and

$$\sigma = \sqrt{\frac{1}{M} \sum_{m=1}^M (I_m - \gamma I_m^{(D)})^2} \quad (12)$$

measures the deviation from uniform convergence to the design intensities. Selecting

$$\gamma = \frac{\sum_{m=1}^M I_m I_m^{(D)}}{\sum_{m=1}^M (I_m^{(D)})^2} \quad (13)$$

minimizes the total error and accounts for non-ideal diffraction efficiency. The weighting fraction  $f$  sets the relative importance attached to diffraction efficiency versus uniformity.

In the simplest direct search for an optimal phase distribution, any candidate change that reduces  $C$  is accepted, and all others are rejected. In a worst-case implementation, the number of trials required for practical convergence should scale as  $NP$ , the product of the number of phase pixels and the number of possible phase values. In practice, this rough estimate is accurate if  $P$  and  $N$  are comparatively small and if the starting phase function is either uniform or purely random. Much faster convergence can be obtained by starting from the phase obtained by superposing the desired beams with random relative phases and ignoring amplitude modulations. In this case, convergence typically is obtained within  $N$  trials, even for fairly complex trapping patterns, and thus requires a computational effort comparable to the initial superposition.

As a practical demonstration, we implement a challenging quasiperiodic array of optical traps. The traps are focused with a  $100\times$  NA 1.4 S-Plan Apo oil immersion objective lens mounted in a Nikon TE-2000U inverted optical microscope. The traps are powered by a Coherent Verdi frequency-doubled diode-pumped solid state laser operating at a wavelength of 532 nm. Computer-generated phase holograms are imprinted on the beam with a Hamamatsu X8267-16 parallel-aligned nematic

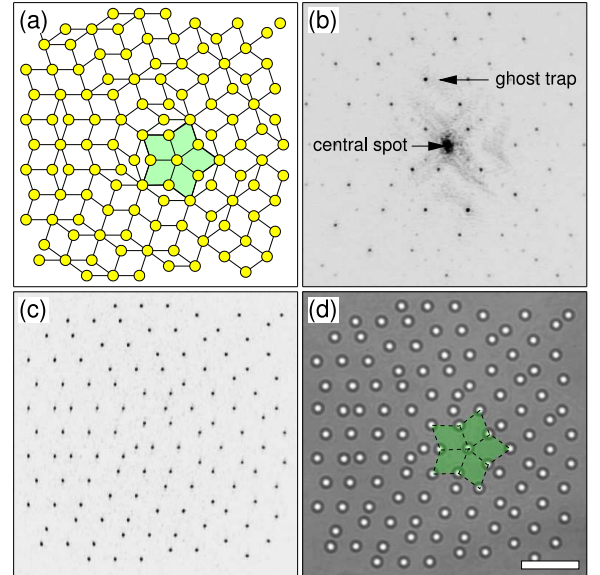


FIG. 2: (a) Design for 119 identical optical traps in a two-dimensional quasiperiodic array. (b) Trapping pattern projected without optimizations using the adaptive-additive algorithm. (c) Trapping pattern projected with optimized optics and adaptively corrected direct search algorithm. (d) Bright-field image of colloidal silica spheres  $1.53 \mu\text{m}$  in diameter dispersed in water and organized in the optical trap array. The scale bar indicates  $10 \mu\text{m}$

liquid crystal spatial light modulator (SLM). This SLM can impose phase shifts up to  $2\pi$  radians at each pixel in a  $768 \times 768$  array. The face of the SLM is imaged onto the objective's 5 mm diameter input pupil using relay optics designed to minimize aberrations. The beam is directed into the objective with a dichroic beamsplitter (Chroma Technologies), which allows images to pass through to a low-noise charge-coupled device (CCD) camera (NEC TI-324AII). The video stream is recorded as uncompressed digital video with a Pioneer 520H digital video recorder (DVR) for processing.

Figure 2(a) shows the intended planar arrangement of 119 holographic optical traps. Even after adaptive-additive refinement, the hologram resulting from simple superposition with random phase fares poorly for this aperiodic pattern. Figure 2(b) shows the intensity of light reflected by a front-surface mirror placed in the sample plane. This image reveals extraneous ghost traps, an exceptionally bright central spot, and large variability in the intended traps' intensities. Imaging photometry on this and equivalent images produced with different random relative phases for the beams yields a typical root-mean-square (RMS) variation of more than 50 percent in the projected traps' brightness. The image in Fig. 2(c) was produced using the modified optical train described in Sec. I and the direct search algorithm described in Sec. II, and suffers from none of these defects. Both the ghost traps and the central spot are suppressed, and the apparent relative brightness variations are smaller than 5 percent, a factor of ten improvement. Figure 2(d) shows 119 colloidal silica spheres,  $2a = 1.5 \pm 0.3 \mu\text{m}$  in diameter (Bangs Labs, lot 5238), dispersed in water at  $T = 27^\circ\text{C}$  and trapped in the quasiperiodic array.

To place the benefits of the direct search algorithm on a more quantitative basis, we augment standard figures of merit with those introduced in Ref. [15]. In particular, the DOE's theoretical diffraction efficiency is commonly defined as

$$\mathcal{Q} = \frac{1}{M} \sum_{m=1}^M \frac{I_m}{I_m^{(D)}}, \quad (14)$$

and its root-mean-square (RMS) error as

$$e_{\text{rms}} = \frac{\sigma}{\max(I_m)}. \quad (15)$$

The resulting pattern's departure from uniformity is usefully gauged as [15]

$$u = \frac{\max(I_m/I_m^{(D)}) - \min(I_m/I_m^{(D)})}{\max(I_m/I_m^{(D)}) + \min(I_m/I_m^{(D)})}. \quad (16)$$

Figure 3 shows results for a HOT DOE encoding 51 traps, including 12 optical vortices of topological charge  $\ell = 8$ , arrayed in three planes relative to the focal plane. The excellent results in Fig. 3 were obtained with a *single* pass of direct-search refinement. The resulting traps, shown in the bottom three images, again vary from their

planned relative intensities by less than 5 percent. In this case, the spatially extended vortices were made as bright as the point-like optical tweezers by increasing their requested relative brightness by a factor of 15. This single hologram, therefore, demonstrates independent control over three-dimensional position, wavefront topology, and brightness of all the traps. Performance metrics for the calculation are plotted in Fig. 3(b) as a function of the number of accepted single-pixel changes, with an overall acceptance rate of 16 percent. Direct search refinement achieves greatly improved fidelity to design over randomly phase superposition at the cost of a small fraction of the diffraction efficiency and roughly doubled computation time. The entire calculation can be completed in the refresh interval of a typical liquid crystal spatial light modulator.

### III. OPTIMAL CHARACTERIZATION

At least numerically, direct search algorithms are both faster and better at calculating trap-forming DOEs than iterative refinement algorithms. The real test, however, is in the projected traps' ability to trap particles. A variety of approaches have been developed for gauging the forces exerted by optical traps. The earliest involved measuring the hydrodynamic drag required to dislodge a trapped particle [16]. This has several disadvantages, most notably that it identifies only the marginal escape force in a given direction and not the trap's actual three-dimensional potential. Most implementations, furthermore, failed to collect sufficient statistics to account for thermal fluctuations' role in the escape process, and did not account adequately for hydrodynamic coupling to bounding surfaces.

Complementary information can be obtained by measuring a particle's thermally driven motions in the trap's potential well [17, 18, 19]. For instance, the measured probability density  $P(\vec{r})$  for displacements  $\vec{r}$  is related to the trap's potential  $V(\vec{r})$  through the Boltzmann distribution

$$P(\vec{r}) \propto \exp(-\beta V(\vec{r})), \quad (17)$$

where  $\beta^{-1} = k_B T$  is the thermal energy scale at temperature  $T$ . Similarly, the power spectrum of  $\vec{r}(t)$  for a harmonically bound particle is a Lorentzian whose width is the viscous relaxation time of the particle in the well [17, 20].

Both of these approaches require amassing enough data to characterize the trapped particle's least probable displacements, and therefore oversample the trajectories. Oversampling is acceptable when data from a single optical trap can be collected rapidly, for example with a quadrant photodiode [17, 18, 19, 21]. Tracking multiple particles in holographic optical traps, however, is most readily accomplished through digital video microscopy [22], which yields data much more slowly. An-

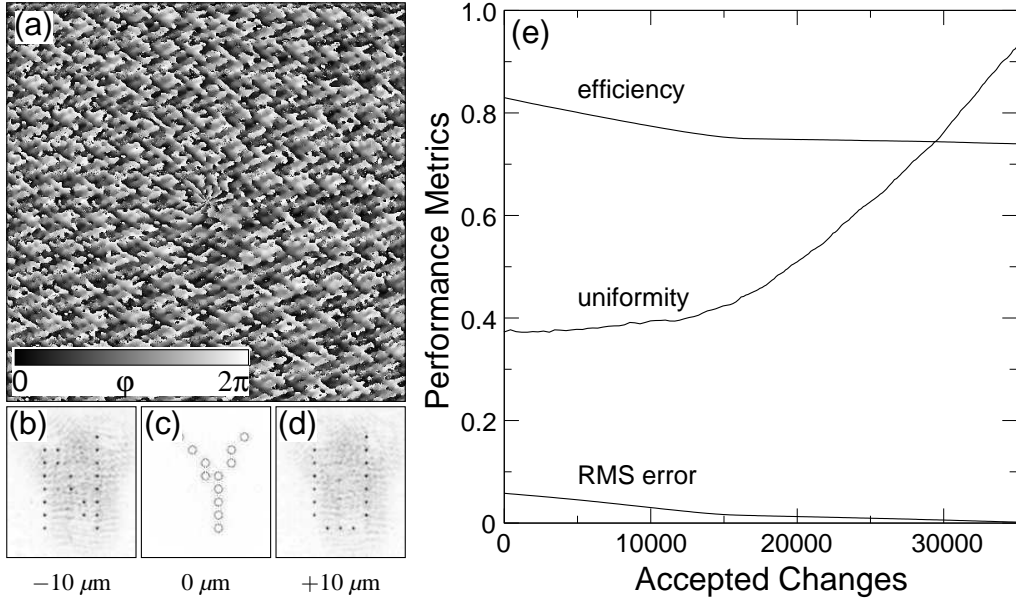


FIG. 3: A three-dimensional multifunctional holographic optical trap array created with the direct search algorithm. (a) Refined DOE phase pattern. (b), (c) and (d) The projected optical trap array at  $z = -10 \mu\text{m}$ ,  $0 \mu\text{m}$  and  $+10 \mu\text{m}$ . Traps are spaced by  $1.2 \mu\text{m}$  in the plane, and the 12 traps in the middle plane consist of  $\ell = 8$  optical vortices. (e) Performance metrics for the hologram in (a) as a function of the number of accepted single-pixel changes. Data include the DOE's overall diffraction efficiency as defined by Eq. (14), the projected pattern's RMS error from Eq. (15), and its uniformity,  $1 - u$ , where  $u$  is defined in Eq. (16).

alyzing video data with optimal statistics [23] offers the benefits of thermal calibration by avoiding oversampling.

An optical trap is accurately modeled as a harmonic potential energy well [18, 19, 20, 21],

$$V(\vec{r}) = \frac{1}{2} \sum_{i=1}^3 \kappa_i r_i^2, \quad (18)$$

with a different characteristic curvature  $\kappa_i$  along each axis. This separable form admits a one-dimensional analysis. The trajectory of a colloidal particle localized in a viscous fluid by a harmonic well is described by the one-dimensional Langevin equation [24]

$$\dot{x}(t) = -\frac{x(t)}{\tau} + \xi(t), \quad (19)$$

where the autocorrelation time  $\tau = \gamma/\kappa$ , is set by the viscous drag coefficient  $\gamma$  and the curvature of the well,  $\kappa$ , and where  $\xi(t)$  describes Gaussian random thermal forcing with zero mean,  $\langle \xi(t) \rangle = 0$ , and variance

$$\langle \xi(t)\xi(s) \rangle = \frac{2k_B T}{\gamma} \delta(t - s). \quad (20)$$

If the particle is at position  $x_0$  at time  $t = 0$ , its trajectory at later times is given by

$$x(t) = x_0 \exp\left(-\frac{t}{\tau}\right) + \int_0^t \xi(s) \exp\left(-\frac{t-s}{\tau}\right) ds. \quad (21)$$

Sampling such a trajectory at discrete times  $t_j = j \Delta t$ , yields

$$\begin{aligned} x_{j+1} &= x_0 \exp\left(-\frac{t_{j+1}}{\tau}\right) \\ &+ \int_0^{t_j} \xi(s) \exp\left(-\frac{t_{j+1}-s}{\tau}\right) ds \\ &+ \int_{t_j}^{t_{j+1}} \xi(s) \exp\left(-\frac{t_{j+1}-s}{\tau}\right) ds \end{aligned} \quad (22)$$

$$= \phi x_j + a_{j+1}, \quad \text{where} \quad \phi = \exp\left(-\frac{\Delta t}{\tau}\right), \quad (23)$$

and where  $a_{j+1}$  is a Gaussian random variable with zero mean and variance

$$\sigma_a^2 = \frac{k_B T}{\kappa} \left[ 1 - \exp\left(-\frac{2\Delta t}{\tau}\right) \right]. \quad (24)$$

Because  $\phi < 1$ , Eq. (23) is an example of an autoregressive process [23], which is readily invertible. In principle, the particle's trajectory  $\{x_j\}$  can be analyzed to extract  $\phi$  and  $\sigma_a^2$ , and thus the trap's stiffness,  $\kappa$ , and the particle's viscous drag coefficient  $\gamma$ .

In practice, however, the experimentally measured particle positions  $y_j$  differ from the actual positions  $x_j$  by random errors  $b_j$ , which we assume to be taken from a Gaussian distribution with zero mean and variance  $\sigma_b^2$ . The measurement then is described by the coupled equations

$$x_j = \phi x_{j-1} + a_j \quad \text{and} \quad y_j = x_j + b_j, \quad (25)$$

where  $b_j$  is independent of  $a_j$ . We still can estimate  $\phi$  and  $\sigma_a^2$  from a set of measurements  $\{y_j\}$  by first constructing the joint probability

$$\begin{aligned}
 p(\{x_i\}, \{y_i\} | \phi, \sigma_a^2, \sigma_b^2) &= \prod_{j=2}^N \left[ \frac{\exp\left(-\frac{a_j^2}{2\sigma_a^2}\right)}{\sqrt{2\pi\sigma_a^2}} \right] \\
 &\times \prod_{j=1}^N \left[ \frac{\exp\left(-\frac{b_j^2}{2\sigma_b^2}\right)}{\sqrt{2\pi\sigma_b^2}} \right] \\
 &= \prod_{j=2}^N \left[ \frac{\exp\left(-\frac{(x_j - \phi x_{j-1})^2}{2\sigma_a^2}\right)}{\sqrt{2\pi\sigma_a^2}} \right] \\
 &\times \prod_{j=1}^N \left[ \frac{\exp\left(-\frac{(y_j - x_j)^2}{2\sigma_b^2}\right)}{\sqrt{2\pi\sigma_b^2}} \right]. \quad (26)
 \end{aligned}$$

The probability density for measuring the trajectory  $\{y_j\}$ , is then the marginal [23]

$$\begin{aligned}
 p(\{y_j\} | \phi, \sigma_a^2, \sigma_b^2) &= \int p(\{x_j\}, \{y_j\} | \phi, \sigma_a^2, \sigma_b^2) dx_1 \cdots dx_N \\
 &= \frac{(2\pi\sigma_a^2\sigma_b^2)^{-\frac{N-1}{2}}}{\sqrt{\sigma_b^2 \det(A_\phi)}} \\
 &\times \exp\left(-\frac{1}{2\sigma_b^2} (\vec{y})^T \left[\mathbf{I} - \frac{A_\phi^{-1}}{\sigma_b^2}\right] \vec{y}\right), \quad (28)
 \end{aligned}$$

where  $\vec{y} = (y_1, \dots, y_N)$ ,  $(\vec{y})^T$  is its transpose,  $\mathbf{I}$  is the  $N \times N$  identity matrix, and

$$A_\phi = \frac{\mathbf{I}}{\sigma_b^2} + \frac{M_\phi}{\sigma_a^2}, \quad (30)$$

with the tridiagonal memory tensor

$$M_\phi = \begin{pmatrix} \phi^2 & -\phi & 0 & 0 & \cdots & 0 \\ -\phi & 1 + \phi^2 & -\phi & 0 & \cdots & \vdots \\ 0 & -\phi & 1 + \phi^2 & -\phi & \cdots & \vdots \\ 0 & 0 & -\phi & \ddots & \cdots & \vdots \\ \vdots & \vdots & \cdots & -\phi & 1 + \phi^2 & -\phi \\ 0 & 0 & \cdots & 0 & -\phi & 1 \end{pmatrix}. \quad (31)$$

Calculating the determinant,  $\det(A_\phi)$ , and inverse,  $A_\phi^{-1}$ , of  $A_\phi$  is greatly facilitated if we artificially impose time translation invariance by replacing  $M_\phi$  with the  $(N+1) \times$

$(N+1)$  matrix

$$\hat{M}_\phi = \begin{pmatrix} 1 + \phi^2 & -\phi & 0 & 0 & \cdots & -\phi \\ -\phi & 1 + \phi^2 & -\phi & 0 & \cdots & \vdots \\ 0 & -\phi & 1 + \phi^2 & -\phi & \cdots & \vdots \\ 0 & 0 & -\phi & \ddots & \cdots & \vdots \\ \vdots & \vdots & \cdots & -\phi & 1 + \phi^2 & -\phi \\ -\phi & 0 & \cdots & 0 & -\phi & 1 + \phi^2 \end{pmatrix}. \quad (32)$$

Physically, this involves imparting an impulse,  $a_{N+1}$ , that translates the particle from its last position,  $x_N$ , to its first,  $x_1$ . Because diffusion in a potential well is a stationary process, the effect of this change is inversely proportional to the number of measurements,  $N$ .

With this approximation, the determinant and inverse of  $A_\phi$  are given by

$$\det(A_\phi) = \prod_{n=1}^N \left\{ \frac{1}{\sigma_b^2} + \frac{1}{\sigma_a^2} \left[ 1 + \phi^2 - 2\phi \cos\left(\frac{2\pi n}{N}\right) \right] \right\} \quad (33)$$

and

$$(A_\phi^{-1})_{\alpha\beta} = \frac{1}{N} \sum_{n=1}^N \frac{\sigma_a^2 \sigma_b^2 \exp(i\frac{2\pi}{N}n(\alpha - \beta))}{\sigma_a^2 + \sigma_b^2 [1 + \phi^2 - 2\phi \cos(\frac{2\pi n}{N})]}, \quad (34)$$

so that the conditional probability for the measured trajectory,  $\{y_j\}$ , is

$$\begin{aligned}
 p(\{y_j\} | \phi, \sigma_a^2, \sigma_b^2) &= (2\pi)^{-\frac{N}{2}} \\
 &\times \prod_{n=1}^N \left\{ \sigma_a^2 + \sigma_b^2 \left[ 1 + \phi^2 - 2\phi \cos\left(\frac{2\pi n}{N}\right) \right] \right\}^{-\frac{1}{2}} \\
 &\times \exp\left(-\frac{1}{2\sigma_b^2} \sum_{n=1}^N y_n^2\right) \\
 &\times \exp\left(-\frac{1}{2\sigma_b^2} \frac{1}{N} \sum_{m=1}^N \frac{\tilde{y}_m^2 \sigma_a^2}{\sigma_a^2 + \sigma_b^2 [1 + \phi^2 - 2\phi \cos(\frac{2\pi m}{N})]}\right), \quad (35)
 \end{aligned}$$

where  $\tilde{y}_m$  is the  $m$ -th component of the discrete Fourier transform of  $\{y_n\}$ . This can be inverted to obtain the likelihood function for  $\phi$ ,  $\sigma_a^2$ , and  $\sigma_b^2$ :

$$\begin{aligned}
 L(\phi, \sigma_a^2, \sigma_b^2 | \{y_i\}) &= -\frac{N}{2} \ln 2\pi \\
 &- \frac{1}{2\sigma_b^2} \sum_{n=1}^N y_n^2 + \frac{\sigma_a^2}{2\sigma_b^2} \frac{1}{N} \sum_{n=1}^N \frac{\tilde{y}_n^2 \sigma_a^2}{\sigma_a^2 + \sigma_b^2 [1 + \phi^2 - 2\phi \cos(\frac{2\pi n}{N})]} \\
 &- \frac{1}{2} \sum_{n=1}^N \ln \left( \sigma_a^2 + \sigma_b^2 \left[ 1 + \phi^2 - 2\phi \cos\left(\frac{2\pi n}{N}\right) \right] \right). \quad (36)
 \end{aligned}$$

Best estimates  $(\hat{\phi}, \hat{\sigma}_a^2, \hat{\sigma}_b^2)$  for the parameters  $(\phi, \sigma_a^2, \sigma_b^2)$

are solutions of the coupled equations

$$\frac{\partial L}{\partial \phi} = \frac{\partial L}{\partial \sigma_a^2} = \frac{\partial L}{\partial \sigma_b^2} = 0. \quad (37)$$

### A. Case 1: No measurement errors ( $\sigma_b^2 = 0$ )

Equations (37) can be solved in closed form if  $\sigma_b^2 = 0$ . In this case,

$$\hat{\phi}_0 = \frac{c_1}{c_0} \quad \text{and} \quad \hat{\sigma}_{a0}^2 = c_0 \left[ 1 - \left( \frac{c_1}{c_0} \right)^2 \right], \quad (38)$$

where

$$c_m = \frac{1}{N} \sum_{j=1}^N y_j y_{(j+m) \bmod N} \quad (39)$$

is the barrel autocorrelation of  $\{y_j\}$  at lag  $m$ . The associated statistical uncertainties are

$$\Delta \hat{\phi}_0 = \sqrt{\frac{\hat{\sigma}_{a0}^2}{N c_0}}, \quad \text{and} \quad \Delta \hat{\sigma}_{a0}^2 = \hat{\sigma}_{a0}^2 \sqrt{\frac{2}{N}}. \quad (40)$$

In the absence of measurement errors,  $c_0$  and  $c_1$  constitute *sufficient statistics* for the time series [23] and thus embody all of the information that can be extracted.

### B. Case 2: Small measurement errors ( $\sigma_b^2 \ll \sigma_a^2$ )

The analysis is less straightforward when  $\sigma_b^2 \neq 0$  because Eqs. (37) no longer are simply separable. The system of equations can be solved approximately if  $\sigma_b^2 \ll \sigma_a^2$ . In this case, the best estimates for the parameters can be expressed in terms of the error-free estimates as

$$\hat{\phi} \approx \hat{\phi}_0 \left\{ 1 + \frac{\sigma_b^2}{\hat{\sigma}_{a0}^2} \left[ 1 - \hat{\phi}_0^2 + \frac{c_2}{c_0} \right] \right\}$$

and

$$\hat{\sigma}_a^2 \approx \hat{\sigma}_{a0}^2 - \frac{\sigma_b^2}{\hat{\sigma}_{a0}^2} c_0 \left[ 1 - 5 \hat{\phi}_0^4 + 4 \hat{\phi}_0^2 \frac{c_2}{c_0} \right], \quad (41)$$

to first order in  $\sigma_b^2/\sigma_a^2$ , with statistical uncertainties propagated in the conventional manner. Expansions to higher order in  $\sigma_b^2/\sigma_a^2$  involve additional correlations, and the exact solution involves correlations at all lags  $m$ . If measurement errors are small enough for Eq. (41) to apply, the computational savings relative to other approaches can be substantial, and the amount of data required to achieve a desired level of accuracy in the physically relevant quantities,  $\kappa$  and  $\gamma$ , can be reduced dramatically.

The errors in locating colloidal particles' centroids can be calculated from knowledge of the images' signal to noise ratio and the optical train's magnification [22].

Centroid resolutions of 10 nm or better can be attained routinely for micrometer-scale colloidal particles in water using conventional bright-field imaging. In practice, however, mechanical vibrations, video jitter and other processes may increase the measurement error. Quite often, the overall measurement error is most easily assessed by increasing the laser power to the optical traps to minimize the particles' thermally driven motions. In this case,  $y_j \approx b_j$ , and  $\sigma_b^2$  can be estimated directly.

### C. Trap characterization

The stiffness and viscous drag coefficient can be estimated simultaneously as

$$\frac{\kappa}{k_B T} = \frac{1 - \hat{\phi}^2}{\hat{\sigma}_a^2}, \quad \text{and} \quad \frac{\gamma}{k_B T \Delta t} = -\frac{1 - \hat{\phi}^2}{\hat{\sigma}_a^2 \ln \hat{\phi}}, \quad (42)$$

with error estimates,  $\Delta \kappa$  and  $\Delta \gamma$ , given by

$$\left( \frac{\Delta \kappa}{\kappa} \right)^2 = \left( \frac{\Delta \hat{\sigma}_a^2}{\hat{\sigma}_a^2} \right)^2 + \left( \frac{2 \hat{\phi}^2}{1 - \hat{\phi}^2} \right)^2 \left( \frac{\Delta \hat{\phi}}{\hat{\phi}} \right)^2 \quad \text{and} \quad (43)$$

$$\left( \frac{\Delta \gamma}{\gamma} \right)^2 = \left( \frac{\Delta \hat{\sigma}_a^2}{\hat{\sigma}_a^2} \right)^2 + \left( \frac{2 \hat{\phi}^2}{1 - \hat{\phi}^2} + \frac{1}{\ln \hat{\phi}} \right)^2 \left( \frac{\Delta \hat{\phi}}{\hat{\phi}} \right)^2. \quad (44)$$

If the measurement interval,  $\Delta t$ , is much longer than the viscous relaxation time  $\tau = \gamma/\kappa$ , then  $\phi$  vanishes and the error in the drag coefficient diverges. Conversely, if  $\Delta t$  is much smaller than  $\tau$ , then  $\phi$  approaches unity and both errors diverge. Consequently, this approach does not benefit from excessively fast sampling. Rather, it relies on accurate particle tracking to minimize  $\Delta \hat{\phi}$  and  $\Delta \hat{\sigma}_a^2$ . For trap-particle combinations with viscous relaxation times exceeding a few milliseconds and typical particle excursions of at least 10 nm, digital video microscopy provides the resolution needed to simultaneously characterize multiple optical traps [22].

In the event that measurement errors can be ignored ( $\sigma_b^2 \ll \sigma_a^2$ ),

$$\frac{\kappa_0}{k_B T} = \frac{1}{c_0} \left[ 1 \pm \sqrt{\frac{2}{N} \left( 1 + \frac{2c_1^2}{c_0^2 - c_1^2} \right)} \right]$$

and

$$\frac{\gamma_0}{k_B T \Delta t} = \frac{1}{c_0 \ln \left( \frac{c_0}{c_1} \right)} \left( 1 \pm \frac{\Delta \gamma_0}{\gamma_0} \right) \quad (45)$$

where

$$N \left( \frac{\Delta \gamma_0}{\gamma_0} \right)^2 = 2 + \frac{1}{c_0^2 - c_1^2} \left[ \frac{c_0^2 + 2c_1^2 \ln \left( \frac{c_1}{c_0} \right) - c_1^2}{c_1 \ln \left( \frac{c_1}{c_0} \right)} \right]^2. \quad (46)$$



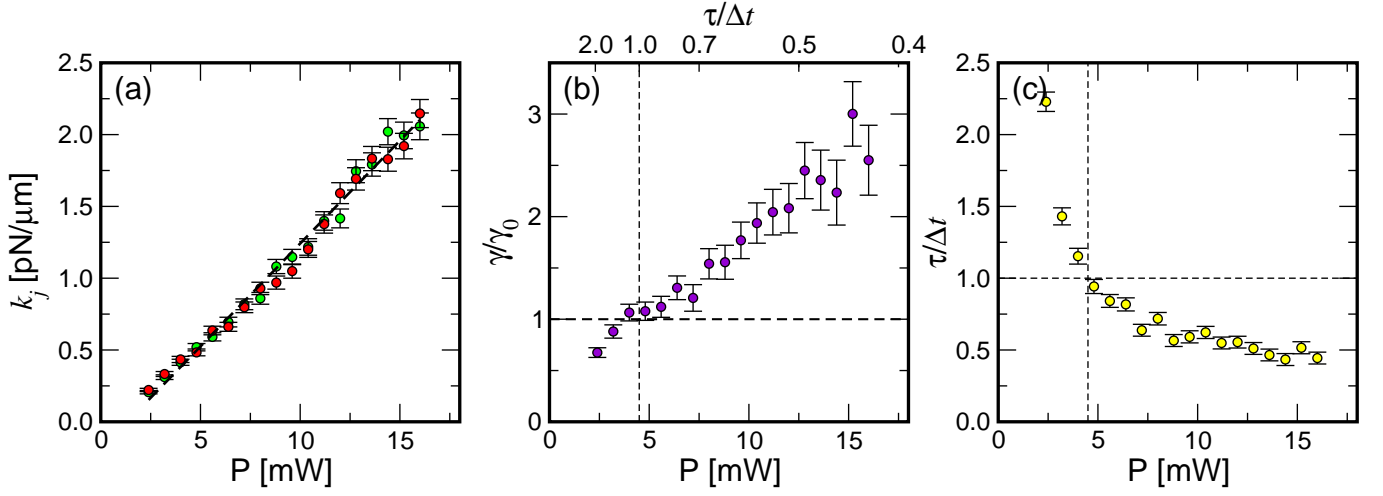


FIG. 4: Power dependence of (a) the trap stiffness, (b) the viscous drag coefficient and (c) the viscous relaxation time for a  $1.53 \mu\text{m}$  diameter silica sphere trapped by an optical tweezer in water.

These results are not reliable if  $c_1 \lesssim \sigma_b^2$ , which arises when the sampling interval  $\Delta t$  is much longer or much shorter than the viscous relaxation time,  $\tau$ . Accurate estimates for  $\kappa$  and  $\gamma$  still may be obtained in this case by applying Eq. (41).

As a practical demonstration of this formalism, we analyzed the thermally driven motions of a single silica sphere of diameter  $1.53 \mu\text{m}$  (Bangs Labs lot number 5328) dispersed in water and trapped in a conventional optical tweezer. With the trajectory resolved to within 6 nm at 1/30 sec intervals, 1 minute of data suffices to measure both  $\kappa$  and  $\gamma$  to within 1 percent error using Eqs. (42). The results plotted in Fig. 4(a) indicate trapping efficiencies of  $\kappa_x/P = \kappa_y/P = 142 \pm 3 \text{ pN}/\mu\text{mW}$ . Unlike  $\kappa$ , which depends principally on  $c_0$ ,  $\gamma$  also depends on  $c_1$ , which is accurately measured only for  $\tau \gtrsim 1$ . Over the range of laser powers for which this condition holds, we obtain the expected  $\gamma_x/\gamma_0 = \gamma_y/\gamma_0 = 1.0 \pm 0.1$ , as shown in Fig. 4(b). The viscous relaxation time becomes substantially shorter than our sampling time for higher powers, so that estimates for  $\gamma$  and for the error in  $\gamma$  both become unreliable, as expected.

#### IV. ADAPTIVE OPTIMIZATION

Optimal statistical analysis offers insights not only into the traps' properties, but also into the properties of the trapped particles and the surrounding medium. For example, if a spherical probe particle is immersed in a medium of viscosity  $\eta$  far from any bounding surfaces, its hydrodynamic radius  $a$  can be assessed from the measured drag coefficient using the Stokes result  $\gamma = 6\pi\eta a$ . The viscous drag coefficients, moreover, provide insights into the particles' coupling to each other and to their environment. The independently assessed values of the traps' stiffnesses then can serve as a self-calibration in

microrheological measurements and in measurements of colloidal many-body hydrodynamic coupling [25]. In cases where the traps themselves must be calibrated accurately, knowledge of the probe particles' differing properties gauged from measurements of  $\gamma$  can be used to distinguish variations in the traps' intrinsic properties from variations due to differences among the probe particles.

These measurements, moreover, can be performed rapidly enough, even at conventional video sampling rates, to permit real-time adaptive optimization of the traps' properties. Each trap's stiffness is roughly proportional to its brightness. So, if the  $m$ -th trap in an array is intended to receive a fraction  $|\alpha_m|^2$  of the projected light, then instrumental deviations can be corrected by recalculating the CGH with modified amplitudes:

$$\alpha_m \rightarrow \alpha_m \sqrt{\frac{\sum_{i=1}^N \kappa_i}{\kappa_m}}. \quad (47)$$

Analogous results can be derived for optimization on the basis of other performance metrics. A quasiperiodic pattern similar to that in Fig. 2(c) was adaptively optimized for uniform brightness, with a single optimization cycle yielding better than 12 percent variance from the mean. Applying Eqs. (42) to data from images such as Fig. 2(d) allows us to correlate the traps' appearance to their actual performance.

With each trap powered by 3.4 mW, the mean viscous relaxation time is found to be  $\tau/\Delta t = 1.14 \pm 0.11$ . We expect reliable estimates for the viscous drag coefficient under these conditions, and the result  $\gamma/\gamma_0 = 0.95 \pm 0.10$  with an overall measurement error of 0.01, is consistent with the manufacturer's rated 10 percent polydispersity in particle radius. Variations in the measured stiffnesses,  $\langle \kappa_x \rangle = 0.38 \pm 0.06 \text{ pN}/\mu\text{m}$  and  $\langle \kappa_y \rangle = 0.35 \pm 0.10 \text{ pN}/\mu\text{m}$ , can be ascribed to a combination of the particles' polydispersity and the traps' inherent brightness variations. This demonstrates that adaptive optimization based on

the traps' measured intensities also optimizes their performance in trapping particles.

## V. SUMMARY

The quality and uniformity of the holographic optical traps projected with the methods described in the previous sections represent a substantial advance over previously reported results. We have demonstrated that optimized and adaptively optimized HOT arrays can be used to craft highly structured potential energy landscapes with excellent fidelity to design. These optimized

landscapes have potentially wide-ranging applications in sorting mesoscopic fluid-borne objects through optical fractionation [11, 12], in fundamental studies of transport [9, 26], dynamics [27, 28] and phase transitions in macromolecular systems, and also in precision holographic manufacturing.

We have benefitted from extensive discussion with Alan Sokal. This work was supported by the National Science Foundation under Grant Number DBI-0233971 with additional support from Grant Number DMR-0451589. S.L. acknowledges support from the Kessler Family Foundation.

- 
- [1] A. Ashkin, J. M. Dziedzic, J. E. Bjorkholm, and S. Chu, *Opt. Lett.* **11**, 288 (1986).
  - [2] E. R. Dufresne and D. G. Grier, *Rev. Sci. Instr.* **69**, 1974 (1998).
  - [3] M. Reicherter, T. Haist, E. U. Wagemann, and H. J. Tiziani, *Opt. Lett.* **24**, 608 (1999).
  - [4] J. Liesener, M. Reicherter, T. Haist, and H. J. Tiziani, *Opt. Comm.* **185**, 77 (2000).
  - [5] E. R. Dufresne, G. C. Spalding, M. T. Dearing, S. A. Sheets, and D. G. Grier, *Rev. Sci. Instr.* **72**, 1810 (2001).
  - [6] J. E. Curtis, B. A. Koss, and D. G. Grier, *Opt. Comm.* **207**, 169 (2002).
  - [7] D. G. Grier, *Nature* **424**, 810 (2003).
  - [8] P. T. Korda, G. C. Spalding, E. R. Dufresne, and D. G. Grier, *Rev. Sci. Instr.* **73**, 1956 (2002).
  - [9] P. T. Korda, M. B. Taylor, and D. G. Grier, *Phys. Rev. Lett.* **89**, 128301 (2002).
  - [10] A. Jesacher, S. Fürhapter, S. Bernet, and M. Ritsch-Marte, *Opt. Express* **12**, 2243 (2004).
  - [11] K. Ladavac, K. Kasza, and D. G. Grier, *Phys. Rev. E* **70**, 010901(R) (2004).
  - [12] M. Pelton, K. Ladavac, and D. G. Grier, *Phys. Rev. E* **70**, 031108 (2004).
  - [13] A. Jesacher, S. Fürhapter, S. Bernet, and M. Ritsch-Marte, *Opt. Express* **12**, 4129 (2004).
  - [14] V. Soifer, V. Kotlyar, and L. Doskolovich, *Iterative Methods for Diffractive Optical Elements Computation* (Taylor & Francis, Bristol, PA, 1997).
  - [15] M. Meister and R. J. Winfield, *Opt. Comm.* **203**, 39 (2002).
  - [16] K. Svoboda, C. F. Schmidt, B. J. Schnapp, and S. M. Block, *Nature* **365**, 721 (1993).
  - [17] L. P. Ghislain, N. A. Switz, and W. W. Webb, *Rev. Sci. Instr.* **65**, 2762 (1994).
  - [18] F. Gittes, B. Schnurr, P. D. Olmsted, F. C. MacKintosh, and C. F. Schmidt, *Phys. Rev. Lett.* **79**, 3286 (1997).
  - [19] E.-L. Florin, A. Pralle, E. H. K. Stelzer, and J. K. H. Hörber, *Appl. Phys. A* **66**, S75 (1998).
  - [20] K. Berg-Sørensen and H. Flyvbjerg, *Rev. Sci. Instr.* **75**, 594 (2004).
  - [21] F. Gittes and C. F. Schmidt, *Opt. Lett.* **23**, 7 (1998).
  - [22] J. C. Crocker and D. G. Grier, *J. Colloid Interface Sci.* **179**, 298 (1996).
  - [23] G. E. P. Box and G. M. Jenkins, *Time Series Analysis: Forecasting and Control* (Holden-Day, San Francisco, 1976).
  - [24] H. Risken, *The Fokker-Planck Equation* (Springer-Verlag, Berlin, 1989), 2nd ed.
  - [25] M. Polin, S. A. Quake, and D. G. Grier, preprint (2005).
  - [26] P. T. Korda, G. C. Spalding, and D. G. Grier, *Phys. Rev. B* **66**, 024504 (2002).
  - [27] S.-H. Lee, K. Ladavac, M. Polin, and D. G. Grier, *Phys. Rev. Lett.* **94**, 110601 (2005).
  - [28] S.-H. Lee and D. G. Grier, *Phys. Rev. E* submitted for publication (2005).